Memristive switching in two-dimensional BiSe crystals

Wenda Ma[1,2], Junfeng Lu[3,4], Shuaipeng Ge[1,2], Li Zhang[2], Fengchang Huang[2], Naiwei Gao[1,2], Peiguang Yan[1] (✉), and Caofeng Pan[1,2] (✉)

[1] College of Physics and Optoelectronic Engineering, Shenzhen University, Shenzhen 518060, China
[2] CAS Center for Excellence in Nanoscience, Beijing Key Laboratory of Micro-nano Energy and Sensor, Beijing Institute of Nanoenergy and Nanosystems, Chinese Academy of Sciences, Beijing 101400, China
[3] College of Physics, Nanjing University of Aeronautics and Astronautics, Nanjing 211106, China
[4] State Key Laboratory of Bioelectronics, Southeast University, Nanjing 210096, China

ABSTRACT

In spite of the explosive rise of research on memristive switching, more improvements in tunability, versatility, and hetero-integration are required through the discovery and application of novel materials. Herein, we report resistance switching in nano-thick two-dimensional (2D) crystals of bismuth selenium (BiSe). The BiSe devices exhibit nonvolatile bipolar resistance switching, volatile switching, and electrical bistable behavior in different conditions. The different memristive behavior of BiSe devices may be related to the concentration of Bi ions in this Bi-rich structure, which directly affects the capability of filaments forming. Furthermore, the external mechanical strain is applied in modulation of multi-layer BiSe devices. The memristive BiSe devices show a large on/off ratio of ~ 10^4 and retention time of ~ 10^4 s. The discovery of memristive switching behavior in multi-layer BiSe is attributed to the forming of Bi filaments. The resistance switching behavior in multi-layer BiSe demonstrates the potential application in the flexible memories and functional integrated devices.

KEYWORDS
bismuth selenium, heterostructure, resistance switching, memristors, flexible memories, strain engineering

1   Introduction

Memristors, the fourth electrical elements, are switchable resistors that vary their internal resistance state based on previously supplied electrical signals [1–3]. Since Chua et al. theoretically proposed the concept in 1971, memristors have been attracting great attention as a novel model for traditional data processing/storage and advanced neuromorphic learning [1, 4–6]. The ability of massive parallel computing is promising to exceed the restrictions of the current von Neumann computing architectures based on the inefficient series connection of processing/storage units [4, 7–9].

Recently, memristive materials, such as metal oxides [10], halides [11, 12], chalcogenides [13], and organic polymers [14, 15], have been widely studied. Among them, two-dimensional (2D) materials, including graphene and h-BN, have attracted considerable interests as an emerging material platform for memristive switching with low power consumption and high performance [4, 16–19]. Compared to bulk materials, 2D materials provide special properties like electrostatic gate tunablity [20], and low-power switching capability [21]. Additionally, 2D materials allow for the creation of devices with diverse functionality [19, 22, 23], and exhibit the mechanical flexibility [24, 25], which fulfills the large requirement for flexible integrated devices in portable and wearable electronics [26]. However, most memristor devices of 2D materials concentrate on much design and modification such as oxidation [27, 28], ionic modulation

[29, 30], grain-boundary engineering [31], polycrystalline design [32], and electrode design [33], etc. At present, only few reports have attempted to implement intrinsic 2D materials directly in memristors. And there is even less work on clearly illustrating the regulatory function of strain in memristors [28, 34]. Hence, it is vital to investigate new 2D material with intrinsically memristive property and uncover its origin. To design novel materials with distinctive structural properties and intrinsically ionic migration, identification of the correlations between formation of filaments and memristive performance has been a significant issue in this field [35]. In addition, strain engineering in 2D memristors, as a novel field, will provide functional integration of devices in the future [36].

Bismuth selenium (BiSe), a member of the homologous $(Bi_2)_m(Bi_2Se_3)_n$ heterostructures (where $m = 1$, $n = 2$) [37], has been discovered as a weak topological insulator [38]. Compared with Bi_2Se_3, BiSe shows n-type electrical conduction, superior electronic transport, and thermoelectric properties [35]. Herein, the multi-layer 2D BiSe single crystal is synthesized by a simple method of chemical vapor deposition (CVD). This Bi-rich Bi_2Se_3 structure may have the potential to form Bi-conducting filaments for memristor performance. Similar metal filaments have also occurred in previous reports. Pandian et al. reported that filamentary resistance switching in $Ge_2Sb_2Te_5$ (GST) is attributed to an excessive amount of Sb elements [39–41]. Yoo et al. observed the Te filament in an amorphous GST thin films [42]. Additionally, Koza et al. reported the superconducting filaments

in δ-Bi$_2$O$_3$, where the observation of superconductivity only occurred when the Bi nanofilaments are formed [43]. Thus, metal ion from 2D material can also lead to memristive bahavior compared to filaments induced by vacancies [44]. In this case, the formation of Bi filaments and the modulation of the strain in multi-layer BiSe devices are investigated systematically.

2   Experimental section

2.1   Synthesis of BiSe nanoflakes

The BiSe nanoflakes were grown via a CVD method using a tube furnace. Commercial Bi$_2$Se$_3$ powder was placed in the center of the furnace tube, which was heated up to 610 °C to offer vapor. The fluorophlogopite mica substrate was positioned downstream, where visible deposition (induced by vapor of Bi$_2$Se$_3$) appeared on the quartz tube. Pure Ar gas with flow rate of 60 sccm was used as the carrier gas. The vapor of Bi and Se atoms was deposited on mica substrates and grown into two types of shapes, triangles, and hexagons. After maintaining 10 min at a pressure of 0.3 kPa, the temperature of the furnace was naturally cooled down to room temperature under a constant Ar flow. Moreover, according to the previous report [45], due to preferential selenium evaporation, after several hours of outgassing, a rather stable flux composition of approximately Bi$_1$Se$_1$ was obtained. The Bi$_2$Se$_3$ phase might be prepared under excess Se condition.

2.2   Transfer of BiSe nanoflakes

The 10 wt.% solution of polystyrene (PS) was prepared by dissolving PS in toluene. The PS solution was spin-coated onto the mica substrate with BiSe nanoflakes. After heating on a hot plate at 95 °C for 15 min, the mica substrate was immersed in water for 30 min (or longer), and then the PS layer with BiSe samples floated on the water surface. Subsequently, the PS-BiSe layer was picked up with a polyethylene terephthalate (PET) substrate and transferred onto PET with the assistance of tweezers. After air drying at room temperature for several hours, the PET substrate adhered with PS-BiSe layer was soaked in N,N-dimethylformamide (DMF) for 20 min to remove the PS layer, and finally the BiSe nanoflakes were transferred onto the PET substrate.

2.3   Fabrication of BiSe devices

The multi-layer BiSe samples were transferred onto a PET substrate. The BiSe terminals were patterned by electron-beam lithography (EBL) process followed by electron-beam evaporation of Cr (10 nm) and Au (40 nm). Afterwards, in order to measure the data under strain, silver paste was applied on both ends of the electrodes and the conductive wires were connected to the BiSe devices. Finally, the BiSe devices were packed inside a layer of hardened epoxy resin.

2.4   Characterization and electrical measurements

The X-ray diffraction (XRD, PANalytical X'Pert3), atomic force microscopy (AFM, MFP-3D-SA), and field-emission scanning electron microscopy (FE-SEM, Quanta 450 equipped with energy dispersive X-ray spectroscopy (EDS) and EBL) were employed to characterize the as-synthesized and transferred BiSe samples. Raman measurement was carried out on Laser Confocal Micro-Raman system (LabRAM HR Evolution) with a 532 nm laser. All electrical measurements were carried out in the dark with a Keithley 4200 Parameter Analyzer. The current–voltage (I–V) curves were measured at a fast sweep mode of Keithley 4200. The static strain applied on BiSe flakes was manipulated by a one-dimensional manual displacement stage presented in Figs. S7(b) and S7(c) in the Electronic Supplementary Material (ESM).

3   Results and discussion

3.1   Growth and characterization of multi-layer BiSe flakes

The synthesis procedure of samples is shown in Fig. 1(a). Few-layer BiSe flakes were synthesized on fluorophlogopite mica (KMg$_3$(AlSi$_3$O$_{10}$)F$_2$) substrates at 0.3 kPa and 610 °C via a CVD method (see the Experimental section for more details). Figures 1(b) and 1(c) show typical optical microscopy images of the multi-layer BiSe flakes prepared on a mica substrate. It is remarkable that these BiSe nanoflakes show two types of shapes, triangles, and hexagons. The side lengths of synthesized triangle flakes are up to 10–40 μm. And BiSe nanoflakes are randomly distributed on a mica substrate. The hexagon flakes are thicker than the triangle flakes. The well-defined shapes indicate the good crystallinity of BiSe flakes. In Fig. 1(d), the layer thickness measured by AFM is shown, confirming a thickness of 10 nm for the BiSe flake. The XRD pattern (Fig. 1(e)) can be identified as that of the layered BiSe structure (space group: $P\bar{3}m1$) [35, 46]. It is noteworthy that two characterization results of X-ray diffraction in the same BiSe sample have appeared with different measured mode in Figs. S1(a) and S1(b) in the ESM. The XRD pattern can be identified as that of the BiSe phase with the 2θ mode, while the XRD pattern was identified as Bi$_2$Se$_3$ phase with the Gonio mode, because the structure of BiSe contains the Bi$_2$Se$_3$.

3.2   Flexible BiSe device and Raman spectrum

Figure 2(a) demonstrates the schematic diagram of BiSe-based memristive device on a flexible PET substrate. The few-layer BiSe flakes with thicknesses ranging from 10 to 40 nm were transferred to the PET substrates. And then two electrodes consisting of chromium and gold (Cr/Au: 10/40 nm thick; 5 μm width) were deposited on the as-transferred BiSe flake. Finally, a flexible BiSe
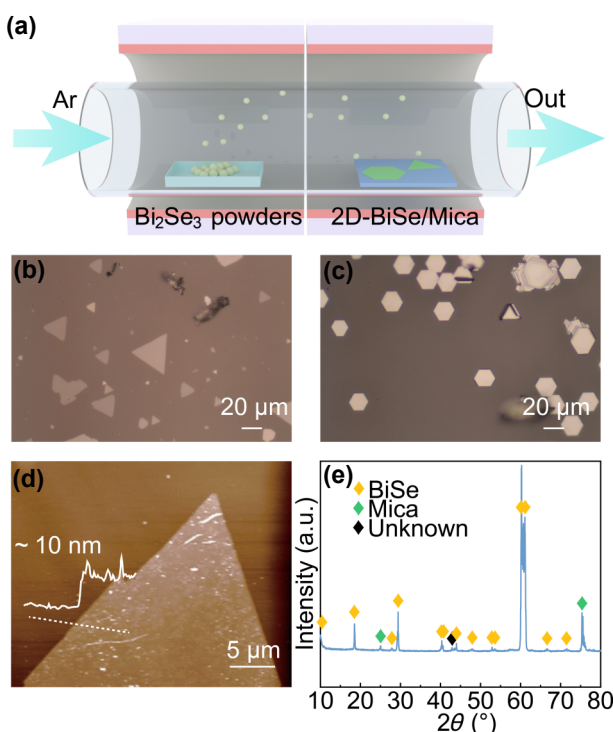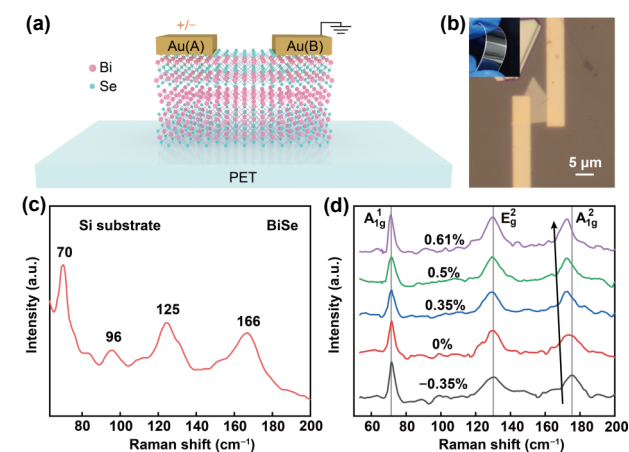

Figure 1 Synthesis, morphology, and structural characterization of BiSe nanoflakes. (a) Schematic diagram of the preparation of BiSe crystals. (b) and (c) Optical micrograph of the multi-layer BiSe samples grown on the mica substrate, in which 2D BiSe flakes show triangle and hexagon shapes. (d) Typical AFM image and height profile of as-grown BiSe flakes. (e) XRD pattern of the multi-layer BiSe.
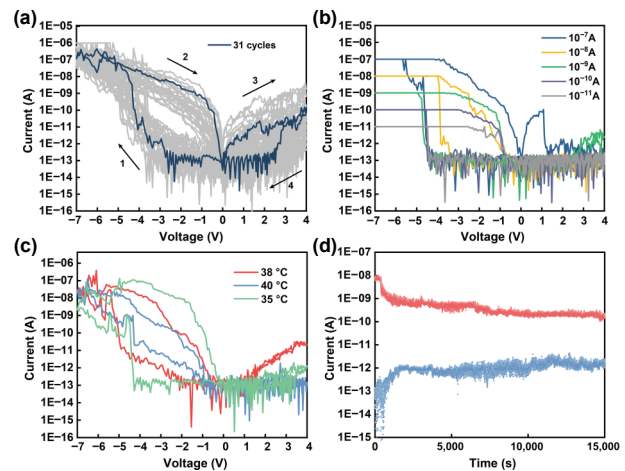
memristive device was prepared. During all electrical measurements, the voltages are applied on the electrode A, while the electrode B is always grounded, as shown in Fig. 2(a). Figure 2(b) demonstrates an optical microscopy image of single BiSe device inserted with a photo of bent PET. The Raman spectrum of multi-layer BiSe shown in Fig. 2(c) contains four characteristic Raman modes at 70, 96, 125, and 166 cm^{-1} on Si substrate, which agrees well with the results of the previous report [47]. However, the Raman spectrum of BiSe on the PET substrate shows three characteristic Raman modes of Bi_2Se_3 assigned to the A_{1g}^1, E_g^2, and A_{1g}^2 modes (Fig. S1(d) in the ESM). Also, different Raman spectrum in the same BiSe sample appears on different substrates. The E_g^2 mode corresponds to the in-plane vibrations of Bi-Se atoms and the A_{1g}^1, A_{1g}^2 modes represent the out-of plane vibrations [27, 48, 49]. As the tensile strain was applied, the A_{1g}^1 and E_g^2 modes remain unchanged, whereas the redshift of A_{1g}^2 mode appears, as shown in Fig. 2(d). The change of the out-of-plane vibrations implies the existence of Bi_2 between Bi_2Se_3 layers.

3.3 Memristive performance of BiSe flakes

In Fig. 3(a), typical *I–V* characteristics of a BiSe flake over a voltage sweep cycle of 0→−7→+4→0 V are plotted at 30 °C, which exhibits bipolar resistance switching behavior. During the negative bias scan, the high resistance state (HRS) is switched to the low resistance state (LRS), which is considered to be the SET process, while during the positive bias scan, the RESET process switches the device from LRS to HRS. The *I–V* curves of a BiSe device show repeatable threshold switching between the HRS and LRS for 31th cycles shown in Fig. 3(a). Additionally, volatile and non-volatile resistive switching can be realized by using controlled compliance currents. Without limiting compliance current, the *I–V* curve shows a non-volatile switching behavior between −4 and −5 V with an on/off ratio as high as ∼ 10^4. As shown in Fig. 3(b), when applying compliance current < 0.1 μA, the nonvolatile resistive switching transforms into the volatile switching. The BiSe device will spontaneously relax back to the HRS in the volatile state. The volatile state can be attributed to Rayleigh instability. The spontaneous diffusion of Bi atoms leads to the dissolution of the filament [50]. However, the initial BiSe samples always keep the high current state without forming of filaments. And the BiSe memristor requires the forming process before measurement. The BiSe sample is first "formed" by gradually increasing the compliance current to break the natural Bi bilayer and produce the new conducting filaments (Fig. S2(a) in the ESM). In general,

Figure 3 Electrical characteristics of BiSe memristors. (a) Typical *I–V* characteristics of a BiSe device. The dark blue line corresponds to the 31th switching process from the LRS to the HRS. (b) *I–V* characteristics of this BiSe device with the different compliance current. (c) Temperature-dependent *I–V* plots. (d) Retention performance of the BiSe device at −2 V.

memristive behavior of BiSe devices should be related to the appropriate concentration of Bi ions. In addition, repeated measurements are applied among the negative region (Fig. S2(b) in the ESM). With increasing measurements, pinched hysteresis loops do not rise, suggesting that 2D BiSe devices are not the mechanism of analog switching function.

Figure 3(c) shows the temperature-dependent *I–V* plots. When the temperature rises to 38 and 40 °C, the on/off ratio of a BiSe device drops dramatically. With the temperature of 30–35 °C, a steep current rise occurred in this BiSe device. The appropriate temperature can promote the better memristive behavior. A retention properties (15,000 s) of both the HRS and LRS of −2 V at 30 °C were shown in Fig. 3(d). The on/off ratio decays from ∼ 10^4 to ∼ 10^2, but the HRS and LRS can still be distinguished. The bending cycle test was performed under ∼ 0.6% compressive strain and both the HRS and LRS exhibited some variation during 200 bending cycles (Fig. S3 in the ESM), which demonstrates the potential application of the BiSe nanoflakes for flexible electronics. The decay of the device may be caused by changes of contact between the electrode and sample under compressive strain, which is worth further optimization and exploration in the future.

3.4 Switching mechanism of BiSe flakes

To explain the resistive switching phenomenon of BiSe flakes, the mechanism in Fig. 4 is proposed. BiSe has a layered crystal structure composed of a bismuth bilayer (Bi_2) sandwiched between two Bi_2Se_3 quintuple layers of Se-Bi-Se-Bi-Se, which is fundamentally a natural heterostructure (Fig. 4(a)). The existence of an additional bismuth bilayer (Bi_2 layer) is predicted to play an essential role in electron conduction and the formation of filament. Koza et al. reports the observation of superconductivity in δ-Bi_2O_3 due to the existence of Bi nanofilaments [43]. Also, the Bi_2Se_3 structure allows the storage and migration of ions and is commonly used as anode of lithium-ion batteries and supercapacitors [51–54], which provides the platform for forming of filaments. After the electroforming and measuring at the LRS, dark contrast areas appear in BiSe (Fig. 4(b)), which remain almost unchanged as the device is switched to the HRS. When this device was washed in acetone, the color changed slightly. Then this device was placed for 1 month in air with the less change of color (Fig. S4 in the ESM). And this dark-contrast region is similar with Ag filaments [28, 55]. This observation indicates some significant composition changes in the formation of a conduction channel. Additionally, EDS mapping is utilized to investigate the

Figure 2 The BiSe memristor and Raman spectrum. (a) Schematic diagram of a BiSe memristive device on a flexible PET substrate. (b) Optical microscopy image of flexible multi-layer BiSe device. Inset: photo of the flexible PET substrate. (c) Raman spectrum of a BiSe flake on Si substrate. (d) Raman spectra of A_{1g}^1, E_g^2, and A_{1g}^2 modes shown on the PET substrate under different strain.
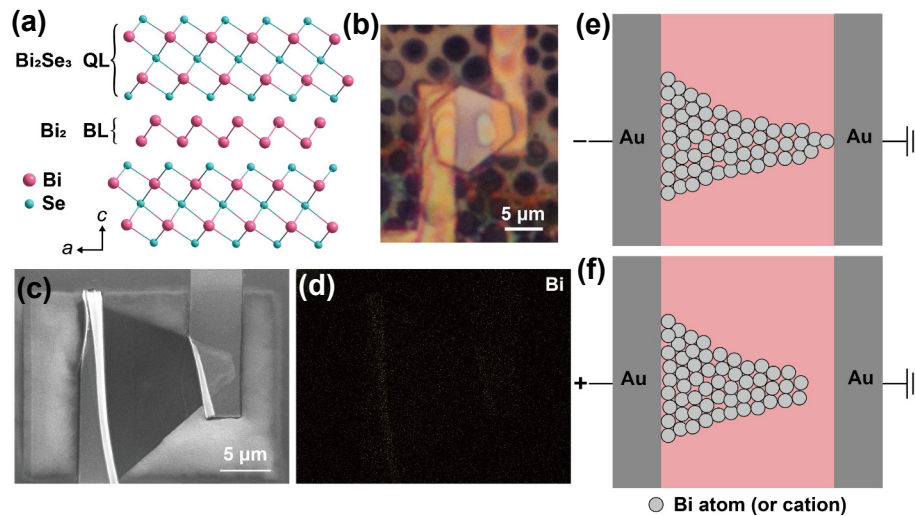
Figure 4 Switching mechanism. (a) A crystal structure schematic diagram of the BiSe. (b) Optical microscopy image of a BiSe device after being programmed to resistance states. (c) SEM image of a BiSe device after switching measurement. (d) EDS elemental mapping of this BiSe device for the elements of Bi, distributed on the Au electrode. (e) and (f) Schematic model of resistive switching at the Bi filaments formation and ruption states.

elemental distribution of the BiSe layer for the HRS, as depicted in Figs. 4(c) and 4(d). Many Bi elements are distributed on Au electrode, verifying the migration of Bi ion in resistance switching process. This observation is consistent with the decreasing contrast in the channel area (Fig. 4(b)). Therefore, the switching mechanism is mainly arisen from the migration of Bi ions. So the change of channel area is considered to be the main reason for the observed high switching performance. When electrode A is probed with negative voltage bias, a number of Bi conductive filaments are established between the two electrodes, resulting in a consequent transition of the device from the HRS to LRS. Because of the high electrochemical activity, Bi is prone to ionize into Bi^{3+} cations, which migrate to the other electrode under external bias. At the same time, the neutral Bi atoms can be reduced from the Bi^{3+} cation, and bridging a conductive path between the two terminals (as shown in Fig. 4(e)). On the contrary, the Bi metallic filaments are dissolved during the reset process when the positive voltage bias is applied. The partial dissolution of the conductive filament at the thinner position leads to the appearance of the HRS. The remnant conductive bridge can be visualized in Fig. 4(f) [55].

Few reports have attempted to illustrate the strain modulation for memristors, because of its low impact on the LRS. In our case, the efficient regulation of BiSe devices was achieved using external mechanical strain. In Fig. S6(a) in the ESM, a good retention can be obtained in some BiSe samples without forming under 0.71% tensile strain, whereas the long-term memory appears at 110th cycle. And the good memristive properties can be regulated by the compressive strain in some decaying BiSe devices (Fig. S6(b) in the ESM). Generally, tensile strain will achieve small current of BiSe devices, while compressive strain will lead to large current of BiSe devices. As the high current is shown in BiSe samples before forming (high Bi concentration), tensile strain is required to reduce the current for easier recovery to a high resistance state. When the low current is shown in decayed devices (low Bi concentration), compressive strain is required to enhance the current to obtain the better switching performance. 2D BiSe is like an electrode. Under tensile strain, the small-sized Bi filaments will crack, leading to a breaking of the connection, while the larger conductive filaments remain and do not break easily. So, the strain can regulate the probability of cracking of all filaments. Similarly, under the tensile strain, the forming of Bi filaments may become more difficult due to the requirement of the higher Bi concentration. The applied tensile/compressive strain is related to

the forming probability of filaments, where the compressive strain can promote the formation of filaments and the tensile strain will decrease the formation of filaments.

3.5 Write-once-read-many-times (WORM) memory regulated by strain

Figure 5(a) presents the *I–V* characteristic of a BiSe device without forming process (compliance current: 1.0×10^{-5} A). Before forming process, the BiSe devices exhibit the electrical bistable behavior, and the WORM memory effect. This observation is similar with the previous reports [56–58]. Starting from the HRS of the device, the current increases sharply from 3.2×10^{-9} to 1.0×10^{-5} A as the applied voltage increases to 2.2 V, suggesting that the electrical performance is converted to the LRS. In the following positive scan (step 2), the device remains in a high conductivity state. Following the reverse sweep to −3.5 V (step 3), the BiSe sample remains in the high conductivity state. And the off resistive state is not recovered (step 4), which demonstrates the inerasable data memory characteristics. In addition, the high conductivity state remains in step 5, indicating the nonvolatile WORM memory characteristics of the BiSe device. This observation can be ascribed to the existence of Bi_2 bilayer. Few reports have attempted to illustrate the recovery of the WORM behavior, because the memory device cannot be electronically rewritten [16]. Wu et al. reported that the high conductivity state was restored by a simple heat treatment in the graphene device [59]. Here, we provide a new approach to recover the WORM device of the BiSe nanoflakes. The applied compressive strain (and release) can recover the LRS of 2D BiSe as shown in Figs. 5(b) and 5(c). The *I–V* characteristic is measured within ±0.1 V. As 0.71% compressive strain was applied, high current (LRS) was still remained. However, when the compressive strain was released to 0%, the low current (HRS) was obtained. Thus, the HRS was recovered from the LRS by applying strain. During this process, the measurement within ±0.1 V will cause the rearrangement of Bi atom, then the cracks of Bi filaments will appear in released process, and leading to the reduction of the current. This HRS obtained by the strain can remain as high as ±1.5 V (shown in Fig. 5(d)). And the HRS obtained by the strain can be maintained over 10^4 s (shown in Fig. 5(e)). The BiSe-based WORM devices exhibit a superior stability in both HRS and LRS with no significant degradation, which was examined by means of continuous retention measurement at −1 V for 10^4 s (Fig. 5(f)). Before forming
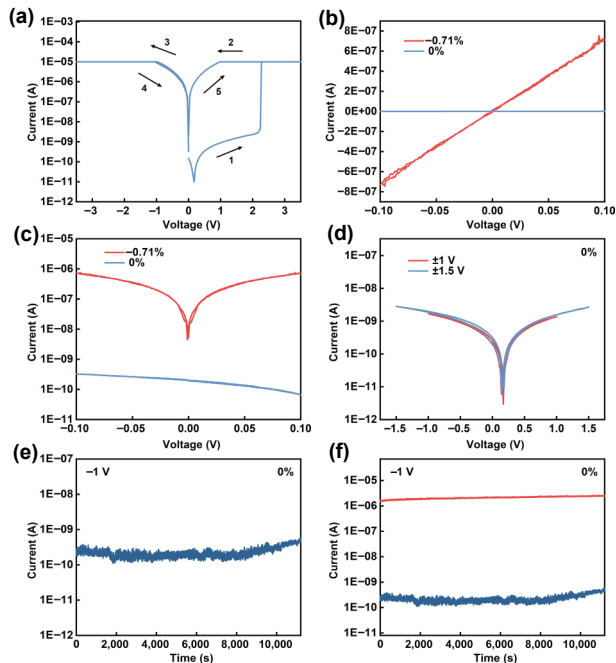
Figure 5 The WORM memory regulated by strain. (a) The first switching process of the initial BiSe without filaments forming. The HRS cannot be automatically regained in the second switching process. (b) and (c) The recovered HRS by 0.71% compressive strain (and release) with *I*–*V* plots within ±0.1 V. (d) The HRS obtained by the strain reaching as high as ±1.5 V. (e) Retention measurement at −1 V for the HRS obtained by the strain. (f) Retention measurement of WORM BiSe sample for the HRS and LRS.

process, the conductive bridges are easily formed in Bi-rich structure, and demonstrating the unerase phenomenon. The compressive strain and release operated in BiSe devices may break the Bi filaments, which overcomes this unerase phenomenon. In the process, the reduced current in Figs. 5(a), 5(d), and 5(f) can be induced by the strain (corresponding to Fig. S3 in the ESM). The recoverable electrical transition makes the BiSe-based device applicable in flexible nonvolatile memories.

4 Conclusions

In summary, we have succeeded in preparing the 2D multi-layer BiSe single crystal through a simple method of CVD. The triangles and hexagons shapes of BiSe nanoflakes showed the good crystallinity. Memory performance and the modulation of the strain were investigated in multi-layer BiSe flexible devices for the first time. The BiSe devices can exhibit nonvolatile bipolar resistance switching, volatile switching, and electrical bistable behavior (nonvolatile WORM memory effect), which is ascribed to the intrinsic Bi bilayer in BiSe structure. The different memristive behavior of BiSe devices is related to the concentration of Bi ions in this Bi-rich structure, which directly affects the capability of filaments forming. The BiSe devices can be evidently regulated by strain, which demonstrates the compressive strain will promote the formation of filaments while the tensile strain will decrease the formation of filaments. And the compressive strain and release operated in BiSe devices may break the Bi filaments, which overcomes the unerase phenomenon. The memristive BiSe device shows a large on/off ratio of $\sim 10^4$ and retention time of $\sim 10^4$ s. The resistance switching behavior in multi-layer BiSe presents superior opportunities to fabricate parallel computing/storage devices, electromechanical sensors, flexible memories, and functional integrated devices.

Acknowledgements

The authors thank the support of the National Natural Science

References

[1] Chua, L. Memristor-the missing circuit element. *IEEE Trans. Circuit Theory* **1971**, *18*, 507–519.

[2] Strukov, D. B.; Snider, G. S.; Stewart, D. R.; Williams, R. S. The missing memristor found. *Nature* **2008**, *453*, 80–83.

[3] Liu, H. T.; Hua, Q. L.; Yu, R. M.; Yang, Y. C.; Zhang, T. P.; Zhang, Y. J.; Pan, C. F. A bamboo-like GaN microwire-based piezotronic memristor. *Adv. Funct. Mater.* **2016**, *26*, 5307–5314.

[4] Huh, W.; Lee, D.; Lee, C. H. Memristors based on 2D materials as an artificial synapse for neuromorphic electronics. *Adv. Mater.* **2020**, *32*, 2002092.

[5] Sun, L. F.; Wang, Z. R.; Jiang, J. B.; Kim, Y.; Joo, B.; Zheng, S. J.; Lee, S.; Yu, W. J.; Kong, B. S.; Yang, H. In-sensor reservoir computing for language learning via two-dimensional memristors. *Sci. Adv.* **2021**, *7*, eabg1455.

[6] Wang, R.; Shi, T.; Zhang, X. M.; Wei, J. S.; Lu, J.; Zhu, J. X.; Wu, Z. H.; Liu, Q.; Liu, M. Implementing *in-situ* self-organizing maps with memristor crossbar arrays for data mining and optimization. *Nat. Commun.* **2022**, *13*, 2289.

[7] Von Neumann, J. First draft of a report on the EDVAC. *IEEE Ann. Hist. Comput.* **1993**, *15*, 27–75.

[8] Han, X.; Xu, Z. S.; Wu, W. Q.; Liu, X. H.; Yan, P. G.; Pan, C. F. Recent progress in optoelectronic synapses for artificial visual-perception system. *Small Struct.* **2020**, *1*, 2000029.

[9] Tong, L.; Peng, Z. R.; Lin, R. F.; Li, Z.; Wang, Y. L.; Huang, X. Y.; Xue, K. H.; Xu, H. Y.; Liu, F.; Xia, H. et al. 2D materials-based homogeneous transistor-memory architecture for neuromorphic hardware. *Science* **2021**, *373*, 1353–1358.

[10] Wong, H. S. P.; Lee, H. Y.; Yu, S. M.; Chen, Y. S.; Wu, Y.; Chen, P. S.; Lee, B.; Chen, F. T.; Tsai, M. J. Metal-oxide RRAM. *Proc. IEEE* **2012**, *100*, 1951–1970.

[11] Choi, J.; Han, J. S.; Hong, K.; Kim, S. Y.; Jang, H. W. Organic–inorganic hybrid halide perovskites for memories, transistors, and artificial synapses. *Adv. Mater.* **2018**, *30*, 1704002.

[12] Zhang, C.; Li, Y.; Ma, C. L.; Zhang, Q. C. Recent progress of organic–inorganic hybrid perovskites in RRAM, artificial synapse, and logic operation. *Small Sci.* **2022**, *2*, 2100086.

[13] Sangwan, V. K.; Jariwala, D.; Kim, I. S.; Chen, K. S.; Marks, T. J.; Lauhon, L. J.; Hersam, M. C. Gate-tunable memristive phenomena mediated by grain boundaries in single-layer MoS$_2$. *Nat. Nanotechnol.* **2015**, *10*, 403–406.

[14] Lin, W. P.; Liu, S. J.; Gong, T.; Zhao, Q.; Huang, W. Polymer-based resistive memory materials and devices. *Adv. Mater.* **2014**, *26*, 570–606.

[15] Liu, L.; Dong, J.; Liu, J.; Liang, Q.; Song, Y. R.; Li, W. H.; Lei, S. B.; Hu, W. P. High-quality two-dimensional metal-organic framework nanofilms for nonvolatile memristive switching. *Small Struct.* **2021**, *2*, 2000077.

[16] Bertolazzi, S.; Bondavalli, P.; Roche, S.; San, T.; Choi, S. Y.; Colombo, L.; Bonaccorso, F.; Samori, P. Nonvolatile memories based on graphene and related 2D materials. *Adv. Mater.* **2019**, *31*, 1806663.

[17] Manzeli, S.; Ovchinnikov, D.; Pasquier, D.; Yazyev, O. V.; Kis, A. 2D transition metal dichalcogenides. *Nat. Rev. Mater.* **2017**, *2*, 17033.

[18] Voiry, D.; Yang, J.; Chhowalla, M. Recent strategies for improving the catalytic activity of 2D TMD nanosheets toward the hydrogen evolution reaction. *Adv. Mater.* **2016**, *28*, 6197–6206.

[19] Chen, F.; Tang, Q.; Ma, T.; Zhu, B. H.; Wang, L. Y.; He, C.; Luo, X. L.; Cao, S. J.; Ma, L.; Cheng, C. Structures, properties, and challenges of emerging 2D materials in bioelectronics and biosensors. *InfoMat* **2022**, *4*, e12299.

[20] Yang, H.; Heo, J.; Park, S.; Song, H. J.; Seo, D. H.; Byun, K. E.; Kim, P.; Yoo, I.; Chung, H. J.; Kim, K. Graphene barristor, a triode device with a gate-controlled Schottky barrier. *Science* **2012**, *336*, 1140–1143.

[21] Kim, S.; Konar, A.; Hwang, W. S.; Lee, J. H.; Lee, J.; Yang, J.; Jung, C.; Kim, H.; Yoo, J. B.; Choi, J. Y. et al. High-mobility and low-power thin-film transistors based on multilayer MoS_2 crystals. *Nat. Commun.* **2012**, *3*, 1011.

[22] Zhang, Q.; Zuo, S. L.; Chen, P.; Pan, C. F. Piezotronics in two-dimensional materials. *InfoMat* **2021**, *3*, 987–1007.

[23] Wu, P. S.; He, T.; Zhu, H.; Wang, Y.; Li, Q.; Wang, Z.; Fu, X.; Wang, F.; Wang, P.; Shan, C. X. et al. Next-generation machine vision systems incorporating two-dimensional materials: Progress and perspectives. *InfoMat* **2022**, *4*, e12275.

[24] Ning, J.; Wang, J.; Li, X. L.; Qiu, T. F.; Luo, B.; Hao, L.; Liang, M. H.; Wang, B.; Zhi, L. J. A fast room-temperature strategy for direct reduction of graphene oxide films towards flexible transparent conductive films. *J. Mater. Chem. A* **2014**, *2*, 10969–10973.

[25] Bao, R. R.; Tao, J.; Pan, C. F.; Wang, Z. L. Piezophototronic effect in nanosensors. *Small Sci.* **2021**, *1*, 2000060.

[26] Zhang, X. Y.; Wen, F. S.; Xiang, J. Y.; Wang, X. C.; Wang, L. M.; Hu, W. T.; Liu, Z. Y. Wearable non-volatile memory devices based on topological insulator Bi_2Se_3/Pt fibers. *Appl. Phys. Lett.* **2015**, *107*, 103109.

[27] Yin, C. J.; Gong, C. H.; Tian, S. Y.; Cui, Y.; Wang, X. P.; Wang, Y.; Hu, Z. H.; Huang, J. W.; Wu, C. Y.; Chen, B. et al. Low-energy oxygen plasma injection of 2D Bi_2Se_3 realizes highly controllable resistive random access memory. *Adv. Funct. Mater.* **2022**, *32*, 2108455.

[28] Wang, M.; Cai, S. H.; Pan, C.; Wang, C. Y.; Lian, X. J.; Zhuo, Y.; Xu, K.; Cao, T. J.; Pan, X. Q.; Wang, B. G. et al. Robust memristors based on layered two-dimensional materials. *Nat. Electron.* **2018**, *1*, 130–136.

[29] Jadwiszczak, J.; Keane, D.; Maguire, P.; Cullen, C. P.; Zhou, Y. B.; Song, H. D.; Downing, C.; Fox, D.; McEvoy, N.; Zhu, R. et al. MoS_2 memtransistors fabricated by localized helium ion beam irradiation. *ACS Nano* **2019**, *13*, 14262–14273.

[30] Zhu, X. J.; Li, D.; Liang, X. G.; Lu, W. D. Ionic modulation and ionic coupling effects in MoS_2 devices for neuromorphic computing. *Nat. Mater.* **2019**, *18*, 141–148.

[31] Wang, X. W.; Wang, B. L.; Zhang, Q. H.; Sun, Y. F.; Wang, E. Z.; Luo, H.; Wu, Y. H.; Gu, L.; Li, H. L.; Liu, K. Grain-boundary engineering of monolayer MoS_2 for energy-efficient lateral synaptic devices. *Adv. Mater.* **2021**, *33*, 2102435.

[32] Sangwan, V. K.; Lee, H. S.; Bergeron, H.; Balla, I.; Beck, M. E.; Chen, K. S.; Hersam, M. C. Multi-terminal memtransistors from polycrystalline monolayer molybdenum disulfide. *Nature* **2018**, *554*, 500–504.

[33] Xu, R. J.; Jang, H.; Lee, M. H.; Amanov, D.; Cho, Y.; Kim, H.; Park, S.; Shin, H. J.; Ham, D. Vertical MoS_2 double-layer memristor with electrochemical metallization as an atomic-scale synapse with switching thresholds approaching 100 mV. *Nano Lett.* **2019**, *19*, 2411–2417.

[34] Jo, S.; Cho, S.; Yang, U. J.; Hwang, G. S.; Baek, S.; Kim, S. H.; Heo, S. H.; Kim, J. Y.; Choi, M. K.; Son, J. S. Solution-processed stretchable Ag_2S semiconductor thin films for wearable self-powered nonvolatile memory. *Adv. Mater.* **2021**, *33*, 2100066.

[35] Samanta, M.; Pal, K.; Pal, P.; Waghmare, U. V.; Biswas, K. Localized vibrations of Bi bilayer leading to ultralow lattice thermal conductivity and high thermoelectric performance in weak topological insulator n-type BiSe. *J. Am. Chem. Soc.* **2018**, *140*, 5866–5872.

[36] Maiti, R.; Patil, C.; Saadi, M. A. S. R.; Xie, T.; Azadani, J. G.; Uluutku, B.; Amin, R.; Briggs, A. F.; Miscuglio, M.; Van Thourhout, D. et al. Strain-engineered high-responsivity $MoTe_2$ photodetector for silicon photonic integrated circuits. *Nat. Photonics* **2020**, *14*, 578–584.

[37] Lind, H.; Lidin, S.; Häussermann, U. Structure and bonding properties of $(Bi_2Se_3)_m(Bi_2)_n$ stacks by first-principles density functional theory. *Phys. Rev. B* **2005**, *72*, 184101.

[38] Majhi, K.; Pal, K.; Lohani, H.; Banerjee, A.; Mishra, P.; Yadav, A. K.; Ganesan, R.; Sekhar, B. R.; Waghmare, U. V.; Kumar, P. S. A. Emergence of a weak topological insulator from the Bi_xSe_y family. *Appl. Phys. Lett.* **2017**, *110*, 162102.

[39] Li, Y.; Zhong, Y. P.; Zhang, J. J.; Xu, X. H.; Wang, Q.; Xu, L.; Sun, H. J.; Miao, X. S. Intrinsic memristance mechanism of crystalline stoichiometric $Ge_2Sb_2Te_5$. *Appl. Phys. Lett.* **2013**, *103*, 043501.

[40] Pandian, R.; Kooi, B. J.; Palasantzas, G.; De Hosson, J. T. M.; Pauza, A. Polarity-dependent reversible resistance switching in Ge-Sb-Te phase-change thin films. *Appl. Phys. Lett.* **2007**, *91*, 152103.

[41] Woo, J.; Jung, S.; Siddik, M.; Cha, E.; Sadaf, S. M.; Hwang, H. Effect of interfacial oxide layer on the switching uniformity of $Ge_2Sb_2Te_5$-based resistive change memory devices. *Appl. Phys. Lett.* **2011**, *99*, 162109.

[42] Yoo, S.; Eom, T.; Gwon, T.; Hwang, C. S. Bipolar resistive switching behavior of an amorphous $Ge_2Sb_2Te_5$ thin films with a Te layer. *Nanoscale* **2015**, *7*, 6340–6347.

[43] Koza, J. A.; Bohannan, E. W.; Switzer, J. A. Superconducting filaments formed during nonvolatile resistance switching in electrodeposited δ-Bi_2O_3. *ACS Nano* **2013**, *7*, 9940–9946.

[44] Yang, Y.; Du, H. Y.; Xue, Q.; Wei, X. H.; Yang, Z. B.; Xu, C. G.; Lin, D. M.; Jie, W. J.; Hao, J. H. Three-terminal memtransistors based on two-dimensional layered gallium selenide nanosheets for potential low-power electronics applications. *Nano Energy* **2019**, *57*, 566–573.

[45] Springholz, G.; Wimmer, S.; Groiss, H.; Albu, M.; Hofer, F.; Caha, O.; Kriegner, D.; Stangl, J.; Bauer, G.; Holý, V. Structural disorder of natural Bi_mSe_n superlattices grown by molecular beam epitaxy. *Phys. Rev. Mater.* **2018**, *2*, 054202.

[46] Kang, M.; Chai, H. J.; Jeong, H. B.; Park, C.; Jung, I. Y.; Park, E.; Cicek, M. M.; Lee, I.; Bae, B. S.; Durgun, E. et al. Low-temperature and high-quality growth of Bi_2O_2Se layered semiconductors via cracking metal-organic chemical vapor deposition. *ACS Nano* **2021**, *15*, 8715–8723.

[47] Kuznetsov, P. I.; Yakushcheva, G. G.; Shchamkhalova, B. S.; Luzanov, V. A.; Temiryazev, A. G.; Jitov, V. A. Metalorganic vapor phase epitaxy of ternary rhombohedral $(Bi_{1−x}Sb_x)_2Se_3$ solid solutions. *J. Cryst. Growth* **2016**, *433*, 114–121.

[48] Zhang, J.; Peng, Z. P.; Soni, A.; Zhao, Y. Y.; Xiong, Y.; Peng, B.; Wang, J. B.; Dresselhaus, M. S.; Xiong, Q. H. Raman spectroscopy of few-quintuple layer topological insulator Bi_2Se_3 nanoplatelets. *Nano Lett.* **2011**, *11*, 2407–2414.

[49] Das, S. K.; Padhan, P. Surface-induced enhanced band gap in the (0001) surface of Bi_2Se_3 nanocrystals: Impacts on the topological effect. *ACS Appl. Nano Mater.* **2020**, *3*, 274–282.

[50] Lu, X. F.; Zhang, Y. S.; Wang, N. Z.; Luo, S.; Peng, K. L.; Wang, L.; Chen, H.; Gao, W. B.; Chen, X. H.; Bao, Y. et al. Exploring low power and ultrafast memristor on p-type van der waals SnS. *Nano Lett.* **2021**, *21*, 8800–8807.

[51] Zhang, J. S.; Sun, J.; Li, Y. B.; Shi, F. F.; Cui, Y. Electrochemical control of copper intercalation into nanoscale Bi_2Se_3. *Nano Lett.* **2017**, *17*, 1741–1747.

[52] Liu, Z. H.; Yao, X.; Shao, J. F.; Zuo, M.; Pi, L.; Tan, S.; Zhang, C. J.; Zhang, Y. H. Superconductivity with topological surface state in $Sr_xBi_2Se_3$. *J. Am. Chem. Soc.* **2015**, *137*, 10512–10515.

[53] Kumari, P.; Singh, R.; Awasthi, K.; Ichikawa, T.; Kumar, M.; Jain, A. Highly stable nanostructured Bi_2Se_3 anode material for all solid-state lithium-ion batteries. *J. Alloys Compd.* **2020**, *838*, 155403.

[54] Chen, Z. Y.; Yang, Y. R.; Ma, Z. H.; Zhu, T.; Liu, L.; Zheng, J.; Gong, X. All-solid-state asymmetric supercapacitors with metal

selenides electrodes and ionic conductive composites electrolytes. *Adv. Funct. Mater.* **2019**, *29*, 1904182.

[55] Wang, Y.; Yang, J.; Wang, Z. P.; Chen, J. R.; Yang, Q.; Lv, Z. Y.; Zhou, Y.; Zhai, Y. B.; Li, Z. X.; Han, S. T. Near-infrared annihilation of conductive filaments in quasiplane $MoSe_2$/Bi_2Se_3 nanosheets for mimicking heterosynaptic plasticity. *Small* **2019**, *15*, 1805431.

[56] Zhang, X.; Lai, Z. C.; Liu, Z. D.; Tan, C. L.; Huang, Y.; Li, B.; Zhao, M. T.; Xie, L. H.; Huang, W.; Zhang, H. A facile and universal top-down method for preparation of monodisperse transition-metal dichalcogenide nanodots. *Angew. Chem., Int. Ed.* **2015**, *54*, 5425–5428.

[57] Huang, X.; Zheng, B.; Liu, Z. D.; Tan, C. L.; Liu, J. Q.; Chen, B.; Li, H.; Chen, J. Z.; Zhang, X.; Fan, Z. X. et al. Coating two-dimensional nanomaterials with metal-organic frameworks. *ACS Nano* **2014**, *8*, 8695–8701.

[58] Lv, W. Z.; Wang, H. L.; Jia, L. L.; Tang, X. X.; Lin, C.; Yuwen, L. H.; Wang, L. H.; Huang, W.; Chen, R. F. Tunable nonvolatile memory behaviors of PCBM-MoS_2 2D nanocomposites through surface deposition ratio control. *ACS Appl. Mater. Interfaces* **2018**, *10*, 6552–6559.

[59] Wu, C. X.; Li, F. S.; Zhang, Y. A.; Guo, T. L. Recoverable electrical transition in a single graphene sheet for application in nonvolatile memories. *Appl. Phys. Lett.* **2012**, *100*, 042105.